

A multiphysics numerical model of oxidation and decomposition in a uranium hydride bed

Michael P. Kanouff, Patricia E. Gharagozloo, Maher Salloum*, Andrew D. Shugard

Sandia National Laboratories, 7011 East Avenue, MS 9409, Livermore, CA 94550, USA

HIGHLIGHTS

- ▶ A multiphysics finite element model was developed for the reaction of oxygen gas and uranium hydride within a hydrogen storage bed.
- ▶ Uranium hydride and oxygen react quickly, forming U_3O_8 and hydrogen gas.
- ▶ The $UD_3 + O_2$ reaction is faster than the $U + O_2$ reaction.
- ▶ The reactions produce material swelling which reduces the bed porosity and permeability.

ARTICLE INFO

Article history:

Received 24 January 2012

Received in revised form

1 May 2012

Accepted 7 May 2012

Available online 18 May 2012

Keywords:

Uranium hydride

Oxidation

Decomposition

Porous media

Heat transfer

Kinetics

ABSTRACT

The reaction of uranium hydride and oxygen gas in a hydrogen storage bed has been studied with multiphysics finite element modeling. The model considers rates of chemical reaction, heat transport, and mass transport within a hydride bed. Three scenarios of oxygen gas injection have been considered and the model predictions are in good agreement with experimental measurements. We find that, under the conditions studied, uranium hydride and oxygen react quickly, forming U_3O_8 and hydrogen gas. We also find that oxidation of uranium hydride to U_3O_8 produces significant material swelling which, in the reactor studied, reduces the bed porosity from 0.60 to 0.39, and decreases the permeability by a factor of almost 20. A simple, yet reasonably general, description of the process is proposed which accounts for the major changes in global bed flow properties. This model may be used to better anticipate the effects of air-ingress accidents on uranium hydride storage beds and possibly also to explore design options for uranium hydride based hydrogen generation systems.

© 2012 Elsevier Ltd. All rights reserved.

1. Introduction

Uranium hydride beds have been used extensively for hydrogen isotope storage; mainly in nuclear facilities where the mild radioactivity of depleted uranium is a relatively minor concern (Ortman et al., 1990; Heung, 1995; Gill et al., 1983; Walther, 1984; Coffin, 1988; Hayashi et al., 2008; Shmayda and Mayer, 1984; Lasser et al., 1999; Antoniazzi et al., 2008; Bowman and Vis, 1990). However, uranium hydride powder is pyrophoric (Totemeier, 2000; Totemeier and Hayes, 1996; Le Guyadec et al., 2010; Longhurst, 1988; Totemeier et al., 1999; Powell, 2004) and this has long raised questions about storage bed response during air-ingress accidents. The air-ingress problem has been studied by different researchers (Heung, 1995; Perevezentsev et al., 1995; Longhurst, 1990; Longhurst and Shmayda, 1995; Longhurst et al., 1992), most notably by Longhurst (1988, 1990), Longhurst et al. (1992). None of the pre-

vious work, however, has included a model that explicitly considers rates of chemical reaction, heat transport, and mass transport within a hydride bed. Consequently, it is difficult to separate these effects and therefore to anticipate the response of hydride beds to significantly different accident scenarios.

Moreover, uranium hydride storage beds could be employed as single-use hydrogen supplies for portable fuel-cells used to power small electronic devices. We suspect that injecting oxygen into a uranium hydride bed could be an effective way to quickly generate hydrogen gas, on-demand, over a broad temperature range, from a compact volume (Shugard et al., 2011). Granted, it is unlikely that uranium hydride would find widespread application, as there are more attractive single-use hydrogen storage materials, for example $NaBH_4$ and $LiAlH_4$ (McWhorter et al., 2011). Nevertheless, there may be instances where depleted uranium lower hydrogen storage density and mild radioactivity are not significant concerns. However, it will be difficult to design such a system without a reasonable model of bed reaction and hydrogen generation.

* Corresponding author. Tel.: +1 925 294 2585.

E-mail address: mnsallo@sandia.gov (M. Salloum).

Due to the complexities of the system and interactions, and limited availability of data and experimental diagnostic techniques, we have elected to study uranium hydride and oxygen (O_2) reactions within a storage bed, using a combination of modeling and experimental methods. The experiments are described by Shugard et al. (2011). In this paper we describe a multiphysics model developed to account for the most significant chemical, thermal, and mass transport phenomena that influence hydrogen production. The model is intended to be a tool that can help understand storage-bed air-ingress accidents and also to help design single-use hydrogen delivery systems. In this study, we present our model, apply it to three oxygen injection cases, and compare the predictions to experimental measurements.

2. Mathematical model formulation

We develop our model based on the reaction of uranium deuteride (UD_3) for consistency with Shugard et al. (2011) who performed experiments using UD_3 instead of uranium hydride (UH_3). The experiments used UD_3 because the resulting deuterium gas (D_2) was easier to detect in the experimental apparatus, thus reducing experimental uncertainty. Moreover, deuterium (D) and protium (H) are isotopes, differing only by atomic mass, we anticipate that the oxidation kinetics of UD_3 and UH_3 are similar; and therefore this model should apply equally well to both UH_3 and UD_3 beds. The dynamic behavior of the reactor and the production of D_2 involve interactions between multiple transport phenomena within the porous bed. As O_2 is injected into the reactor, chemical reactions including both UD_3 oxidation and decomposition take place. The oxidation reactions release significant amounts of heat and produce D_2 gas. The decomposition reactions consume heat, release D_2 gas and produce uranium (U) metal (which is later oxidized by additional O_2). Within the model domain, coupled transport phenomena are explicitly simulated to predict the thermal response of the reactor surface and the states of the source and exiting gas. The mathematical model is thus comprised by the governing equations for momentum, energy and mass transport, and the chemical reactions. Unless otherwise stated, the units used in the formulation are CGS.

2.1. Model geometry

The geometric model of the reactor is shown in Fig. 1. The features and sizes replicate the experimental study of Shugard et al. (2011). The domain is axisymmetric and includes the O_2 source bottle, the flow channel connecting it to the UD_3 reactor bed, the two frits, a short length of the exiting flow channel, and the reactor wall. The reactor housing is stainless steel. In the experiments, the pressure was monitored at the gas outflow location shown in Fig. 1. This measured pressure signal is used as a pressure boundary condition in the simulations. Gas-tight seals (0.1 cm long) were included in the experiments at the outer surface of the reactor housing. The contact between these seals and the reactor is simulated as a convection-like boundary condition. Two thermocouples were attached to the outer surface of the reactor wall in the experiments, as shown in Fig. 1. TC#1 and TC#2 were located upstream and downstream of the UD_3 bed, respectively. The temperatures predicted by the model at these locations were compared to the measured results from the experiments. Additional details about the experimental setup are available in the study of Shugard et al. (2011).

The computational domain is divided into four sub-domains: the O_2 source and flow channels (Ω_1), the UD_3 reactor bed (Ω_2), the frits at the reactor entrance and exit (Ω_3), and the reactor stainless

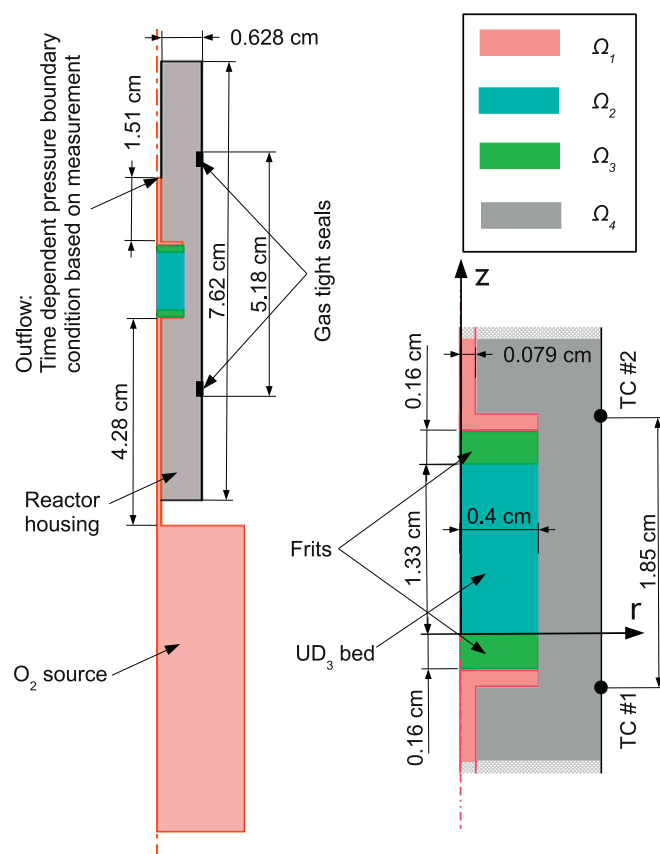


Fig. 1. A schematic of the axisymmetric computational domain of the reactor model. The schematic shows: (left) the entire modeled domain composed of the O_2 source and flow channels (Ω_1), the UD_3 reactor bed (Ω_2), the frits at the reactor entrance and exit (Ω_3), and the reactor stainless steel housing (Ω_4); and (right) a magnified view of the reactor. The temperature is monitored in the experiments at two locations TC#1 and TC#2 at the reactor housing outer surface (Shugard et al., 2011).

steel housing (Ω_4). The thermophysical properties involved in the governing equations (described in the next section) are not the same for each of these sub-domains.

2.2. Governing equations

The release of D_2 from the reactor begins with the injection of O_2 . Modeling this process requires an equation describing momentum transport. The gas flow paths include the open channels, porous media, and frits: Ω_1 , Ω_2 , and Ω_3 , respectively (see Fig. 1), where Ω_2 provides the dominant restriction to gas flow. Many different forms of equations have been developed for describing flow through porous media (Vafai, 2005; Mason and Malinauskas, 1983). In our case, the flow is laminar with a Reynolds number of about 0.02, hence the flowing gas inertia is neglected. Given the large size of the porous UD_3 bed compared to the pore size, we neglect the domain boundary effects. Under these assumptions, Darcy's law appropriately simulates the flow of the O_2 – D_2 gas mixture in the UD_3 bed (Khaled and Vafai, 2003). Darcy's equation is given by:

$$\frac{\partial(\rho_{\text{gas}}\phi)}{\partial t} - \nabla \cdot \left(\frac{\kappa \rho_{\text{gas}}}{\mu} \nabla P \right) = S, \quad \text{in } \Omega_1, \Omega_2, \text{ and } \Omega_3, \quad (1)$$

where ρ_{gas} and μ are the gas density and dynamic viscosity, respectively, P is the gas pressure, and ϕ and κ are the bed porosity and permeability, respectively, assumed to be isotropic. The source term S on the right-hand side of the equation accounts for the consumption of O_2 and the production of D_2 gas phase

within the UD_3 bed Ω_2 ($S=0$ in Ω_1 and Ω_3). Note that the gas is pure O_2 in the Ω_1 region upstream of Ω_2 while it is a D_2 – O_2 mixture inside Ω_2 and in the Ω_1 region downstream of Ω_2 . Although the Navier–Stokes equation is more appropriate for describing gas flow through the open channel portions of the system, the flow restrictions in Ω_1 are negligible compared to the bed, making the details of the viscous and inertial forces in those regions negligible to the system behavior. Consequently, Darcy's equation was used to describe momentum transport in all portions of the system, where a very large permeability (10^{-3} cm^2) was selected for Ω_1 . This assumption induces ill-conditioning in the finite element equations system (Antonio et al., 2003). However, the errors associated with this ill-conditioning are negligible due to the relatively small size of the open channels compared to the domain, and the negligible pressure gradient in the O_2 bottle.

Heat transfer occurs by both convection and conduction. Within the porous medium, the gas and solid phases are assumed to have the same temperature at any given point and time in Ω_2 . The following heat conduction–convection equation describes the heat transfer:

$$(\rho c_p)_{bed} \frac{\partial T}{\partial t} + (\rho c_p)_{gas} \mathbf{V} \cdot \nabla T = \nabla \cdot (k_{bed} \nabla T) + Q, \quad \text{in } \Omega_1, \Omega_2, \Omega_3, \text{ and } \Omega_4, \quad (2)$$

where T is the temperature, \mathbf{V} is the gas velocity vector, and k is the material thermal conductivity. Note that the second term on the left-hand side describing convection uses the density and specific heat of the gas because it is the phase that is in motion. The thermal inertia term (first term on left-hand side) and the conduction term (first term on right-hand side) use the properties of the solid phase because they are much larger than the corresponding gas phase values. The source term Q accounts for heat generation by the chemical reactions in the UD_3 bed Ω_2 ($Q=0$ in Ω_1 , Ω_3 , and Ω_4).

The gas in this system is a mixture of two species, O_2 and D_2 . Transport of the individual species occurs by convection and diffusion, as described by Bird et al. (1960):

$$\frac{\partial c}{\partial t} + \nabla \cdot (c\mathbf{V}) = \nabla \cdot \left[n \mathcal{D} \nabla \left(\frac{c}{n} \right) \right] + R_{O_2}, \quad \text{in } \Omega_1, \Omega_2, \text{ and } \Omega_3, \quad (3)$$

where c is the molar concentration of O_2 , \mathcal{D} is the diffusivity of O_2 in D_2 and n is the molar concentration of the gas. n is the sum of the D_2 and O_2 concentrations such that:

$$n = c + \frac{\rho_{gas} - cM_{O_2}}{M_{D_2}}, \quad (4)$$

where M_{O_2} and M_{D_2} are the molar masses of O_2 and D_2 , respectively. The mass concentration of O_2 is calculated by multiplying c by M_{O_2} . The distribution of the mass concentration of D_2 is then given by $\rho_{gas} - cM_{O_2}$. Note that the convection term is in conservative form i.e., the divergence operator acts on the product of concentration and velocity, which is necessary due to the variability of the total gas density. The source term R_{O_2} (second term on right-hand side) accounts for the consumption of O_2 in the hydride material.

The consumptions of UD_3 and U are described by the conservation equations:

$$\frac{d[UD_3]}{dt} = R_{UD_3}, \quad \text{in } \Omega_2, \quad (5)$$

$$\frac{d[U]}{dt} = R_U, \quad \text{in } \Omega_2, \quad (6)$$

where the transport of these two species either by diffusion or by mechanical deformation is neglected. The distribution of the triuranium octoxide material (U_3O_8) is given by:

$$[U_3O_8] = \frac{[UD_3]^0 - [UD_3] - [U]}{3}, \quad (7)$$

where $[UD_3]^0$ is the initial molar concentration of UD_3 in the reactor bed.

2.3. Chemical reactions

A set of three chemical reactions is assumed to take place in the UD_3 material. First, the decomposition of UD_3 takes place to form U and D_2 following:



The rate of this reaction is assumed to follow a standard Arrhenius form:

$$R_8 = \alpha [UD_3] e^{-\theta/T}, \quad (9)$$

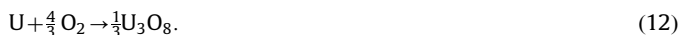
where $\alpha = 14,003 \text{ s}^{-1}$, $\theta = 8630 \text{ K}$ based on the experiments of Condon (Condon and Larson, 1973; Condon, 1980). These values correspond to an activation energy of 17.1 kcal/mol which is consistent with the value measured by Lindner (1990) and the value computed by Balasubramanian et al. (2003). The reaction in Eq. (8) is assumed to take place only when P_{D_2} , the local partial pressure of D_2 is less than P_{eq} , the temperature dependent equilibrium pressure given in torr by Lindner (1990):

$$\log_{10}(P_{eq}(\text{torr})) = 9.14 - 4410/T. \quad (10)$$

P_{D_2} can be calculated in torr by:

$$P_{D_2}(\text{torr}) = 7.5 \times 10^{-4} \frac{\mathcal{R}T}{M_{D_2}} (\rho_{gas} - cM_{O_2}), \quad (11)$$

where $\mathcal{R} = 8.314 \text{ J mol}^{-1} \text{ K}^{-1}$ is the ideal gas constant. The enthalpy change for this reaction is $\Delta H_8 = 128 \text{ kJ/mol}$ of UD_3 (endothermic) (Abraham and Flotow, 1955; Manchester and San-Martin, 1995; Lide, 2004). The second chemical reaction is the oxidation of U given by:



Finally, the third reaction is given by the sum of the reactions in Eqs. (8) and (12):



The preceding equation follows from the study of Powell (2004) that was confirmed by our experimental observations (Shugard et al., 2011). These experiments suggest that UD_3 reacts with O_2 at room temperature and below, where the decomposition rate is very small. Thus, only hydride material would have been present, and no U . To explain the experimental result, direct oxidation of the hydride material is assumed to take place.

Note that, while there are several known uranium oxides: UO_2 , U_3O_7 , U_4O_9 , U_3O_8 , and UO_3 , in Eqs. (12) and (13), only U_3O_8 is assumed to form. This assumption is based mainly on experimental measurements of the amount of O_2 that was absorbed by the hydride material and the amount of D_2 that exited the reactor. That is, when a dose of O_2 was introduced under slow reaction conditions, the measured ratio of D_2 released to O_2 absorbed was closer to $1\frac{1}{8}$, corresponding to the formation of U_3O_8 , than it was to $1\frac{1}{2}$, corresponding to the formation of UO_2 (i.e., $UD_3 + O_2 \rightarrow UO_2 + \frac{3}{2}D_2$) (Shugard et al., 2011).

In addition, the assumption is further supported by McEachern and Taylor's review of UO_2 oxidation, McEachern and Taylor (1998), which indicates that when UO_2 reacts with air or oxygen, U_3O_8 should be the major oxidation product at temperatures important to this model (i.e. between 250 and 1100 °C). If one uses this model in situations where the maximum predicted bed temperatures are not within this range, then this assumption should be reconsidered. Temperatures below 250 °C are expected to favor UO_2 formation whereas U_3O_8 is known to decompose at temperatures above 1100 °C.

Direct oxidation of uranium hydride has received very little attention in the literature. The small amount of work that has been done is not quantitative in terms of reaction rate (Robinson and Thomas, 1996; Epstein et al., 1996; Totemeier, 2000; Powell, 2004). The experiments carried out by our group (Shugard et al., 2011) did not provide quantitative reaction rate data either, however, they did appear to show that the reaction rate at cold temperatures (-60°C) was just as rapid as at room temperature. Given the lack of uranium hydride oxidation rate studies, one may apply kinetic expressions derived for uranium oxidation, expecting that, perhaps, oxidation rates are similar for the metal and hydride. We performed simulations using the U oxidation rates determined by Ritchie (1981). Ritchie's rate expressions were found to predict essentially no reaction at room temperature, even when considering the large specific surface area of the hydride powder. This prediction is inconsistent with our experimental observations and therefore we conclude that, at ambient and sub-ambient temperatures, uranium hydride oxidizes more rapidly than U.

In this work, we estimated the kinetic parameters by fitting the model to experimental results. During the third injection experiment (Shugard et al., 2011), the gas composition exiting the reactor in the reactor transitioned from D_2 to O_2 . The model showed that the effective reaction rate increased with the rate of this gas composition transition. This provided data for estimating the kinetic parameters. The range of O_2 injection rates used in the experiments provided additional data for determining the kinetic parameters. The model showed that the temperatures in the bed increased with the injection rate, thus, the reaction rate increased with increasing injection rate. In the experiments that used slow injection rates, resulting in lower temperatures and slower reaction rates, no O_2 was observed to exit the reactor. This provided evidence for the minimum reaction rate. Since the collection of experiments resulted in a range of bed temperatures, the activation energy and pre-exponential factor in an Arrhenius kinetic mechanism could be individually determined, albeit crudely.

The rate expression for the reaction in Eq. (13) takes the form:

$$R_{13} = \beta f_{\text{O}_2} [\text{UD}_3] e^{-E/RT}, \quad (14)$$

where β was set to 4.38 s^{-1} and the activation energy E was set to $16.63 \text{ kJ mol}^{-1}$ to best match the experimental data. The factor f_{O_2} reflects the availability of O_2 , where it is equal to unity when O_2 is abundant, and it goes to zero if the local O_2 concentration goes to zero. Specifically, f_{O_2} ramps from unity to zero as the local partial pressure of O_2 goes from 200 torr to zero. This is based on work reviewed by Ritchie (1981), which showed little dependence on the partial pressure of O_2 for pressures above 200 torr. The expression for the oxidation of U, R_{12} is identical to R_{13} where the concentration $[\text{U}]$ is used in place of the concentration $[\text{UD}_3]$. Note that the value of the activation energy given by Ritchie (1981) is $76.62 \text{ kJ mol}^{-1}$, much larger than the value of $16.63 \text{ kJ mol}^{-1}$ used here. The large value used by Ritchie for E cannot explain both the complete consumption of O_2 observed in the slow O_2 injection experiments, and the rate of transition of the gas composition observed in the final, faster O_2 injection rate, experiment.

The enthalpies of reaction for reactions (12) and (13) are $\Delta H_{12} = 1085 \text{ kJ/mol}$ of U, and $\Delta H_{13} = 957 \text{ kJ/mol}$ of UD_3 , respectively (exothermic) (Lide, 2004). The source terms in the transport equations can now be identified. In Eq. (1) it is given by:

$$S = \frac{3}{2} M_{\text{D}_2} (R_8 + R_{13}) - \frac{4}{3} M_{\text{O}_2} (R_{12} + R_{13}). \quad (15)$$

The first term accounts for the production of D_2 , on a mass concentration basis, by the reactions of Eqs. (8) and (13). The second term accounts for the consumption of O_2 by the reactions of Eqs. (12) and (13). The heat source term in the energy

equation (2) is given by:

$$Q = \sum_{i=8,12,13} \Delta H_i R_i. \quad (16)$$

The source term in the O_2 transport Eq. (3) is:

$$R_{\text{O}_2} = -\frac{4}{3}(R_{12} + R_{13}). \quad (17)$$

Finally, the source terms for the solid phase conservation Eqs. (5) and (6) are:

$$R_{\text{UD}_3} = -R_8 - R_{13}, \quad (18)$$

$$R_{\text{U}} = -R_8 - R_{12}. \quad (19)$$

R_{O_2} , R_{UD_3} and R_{U} are expressed on a molar basis.

3. Numerical implementation

3.1. Physical properties

The D_2 – O_2 gas mixture flowing in the reactor bed, frits and channels is assumed to obey the ideal gas law. Combining Eq. (4) with the ideal gas equation yields an expression for the gas density ρ_{gas} as a function of pressure, temperature, and composition.

$$\rho_{\text{gas}} = \frac{P}{RT} M_{\text{D}_2} + c(M_{\text{O}_2} - M_{\text{D}_2}). \quad (20)$$

The solid phase density of the powder bed is evaluated as:

$$\rho_{\text{bed}} = n_{\text{bed}} M_{\text{bed}}, \quad (21)$$

where n_{bed} is the total molar density of the bed and can be evaluated as:

$$n_{\text{bed}} = \frac{1}{3}([\text{UD}_3]^0 + 2[\text{UD}_3] + 2[\text{U}]), \quad (22)$$

and M_{bed} is the molecular weight of the bed calculated as:

$$M_{\text{bed}} = \sum_{i=\text{UD}_3, \text{U}, \text{U}_3\text{O}_8} M_i x_i, \quad (23)$$

where $x_i = [i]/n_{\text{bed}}$ is the molar fraction of species i .

The thermal properties of the solid and gas species were obtained from Edwards (1969). Solid phase specific heats were assumed to be constant with the exception of composition effects. The specific heat of a solid mixture per unit mass is evaluated as:

$$c_{p,\text{bed}} = \frac{\sum_{i=\text{UD}_3, \text{U}, \text{U}_3\text{O}_8} C_{p,i} x_i}{\sum_{i=\text{UD}_3, \text{U}, \text{U}_3\text{O}_8} M_i x_i}, \quad (24)$$

where $C_{p,i}$ is the specific heat of the solid species i on a molar basis. Temperature dependent expressions were assumed for the gas species specific heat. The specific heat of the gas mixture is:

$$c_{p,\text{gas}} = \sum_{i=\text{O}_2, \text{D}_2} \frac{\rho_i}{\rho} c_{p,i}. \quad (25)$$

A temperature dependent thermal conductivity is used for the gas, independent of gas composition, and is given by a power law expression:

$$k_{\text{gas}} (\text{W cm}^{-1} \text{ K}^{-1}) = 1.63 \times 10^{-4} \left(\frac{T}{273} \right)^{0.73}. \quad (26)$$

A constant thermal conductivity was used for the bed with a value of $0.01 \text{ W cm}^{-1} \text{ K}^{-1}$, and a value for the frits equal to the product of solid volume fraction (70%) and the conductivity of bulk stainless steel, giving $0.1 \text{ W cm}^{-1} \text{ K}^{-1}$.

The diffusivity of hydrogen in O_2 is pressure and temperature dependent:

$$D = \frac{1.25}{P(\text{atm})} \left(\frac{T}{400} \right)^{1.404}. \quad (27)$$

The gas viscosity was taken from White (1991), and is assumed to be temperature and composition dependent. It is given by:

$$\mu = \sum_{i=O_2, D_2} \mu_i x_i \left(\frac{T}{273} \right)^{0.68}, \quad (28)$$

where μ_i is the viscosity of each species. The density, molecular weight, specific heat, and viscosity are given below in Table 1 for the solid and gas species.

3.1.1. Permeability

The permeability of the hydride powder bed was modeled as a function of the local Knudsen number Kn , as described by Young and Todd (2005):

$$\kappa = \frac{\phi d_p^2}{\tau^2} \left(\frac{1}{32} + \frac{5}{12} Kn \right), \quad (29)$$

where ϕ is the porosity, d_p is the characteristic pore size, and τ is the characteristic tortuosity. In this case, the Knudsen number $Kn = \lambda/d_p$ is the ratio between the gas mean free path, λ , and the characteristic pore size. The mean free path is given by:

$$\lambda = \frac{RT}{\pi \sqrt{2} N_A P d_{O_2}^2}, \quad (30)$$

where $N_A = 6.023 \times 10^{23} \text{ mol}^{-1}$ is Avogadro's number and $d_{O_2} = 3.56 \times 10^{-8} \text{ cm}$ is the O_2 molecule diameter. This latter was assumed to be the biggest molecular diameter among the gas species. This assumption incurs a negligible error in the value of the permeability because the free molecular flow has a relatively small contribution to the final value of κ . The same relationship of Eq. (29) was used for the permeability of the frits, but with different values for ϕ , d_p and τ . The initial porosity ϕ_0 of the bed is based on the measured U loading of the reactor (Shugard et al., 2011) (assuming the material to be fully hydrided), the bulk density of UD_3 , and the dimensions of the bed volume in the reactor, giving $\phi_0 = 0.605$. Starting from that initial value, changes to the porosity are based on the oxide content, because uranium oxide has a much lower bulk density than UD_3 . Consequently, conservation of mass in a constant volume requires that the oxide phase expands and occupies more of the bed volume, such that the porosity decreases. For example, based on the bulk densities of UD_3 and uranium oxide, and the initial porosity, the porosity for the fully oxidized bed is $\phi_1 = 0.393$.

It is assumed that the bed maintains a mechanical equilibrium. Although oxide forms in one part of the bed, we assume that the resulting solid phase expansion creates stresses that compress the remainder of the bed such that ϕ , d_p and τ remain uniform throughout the bed at all times. Then the porosity of the bed may be expressed as:

$$\phi = 1 - (1 - \phi_0)(1 + F\Delta v), \quad (31)$$

where F is the fraction of the bed that is oxide and $\Delta v = 0.536$ is the volume expansion of the oxide phase relative to the hydride phase. The pore size and tortuosity are expressed in terms of the

porosity as:

$$\frac{\phi - \phi_0}{\phi_1 - \phi_0} = \left(\frac{d_p - d_{p,0}}{d_{p,1} - d_{p,0}} \right)^{n_d}, \quad (32)$$

$$\frac{\phi - \phi_0}{\phi_1 - \phi_0} = \left(\frac{\tau - \tau_0}{\tau_0 - \tau_0} \right)^{n_\tau}, \quad (33)$$

where the subscripts 0 and 1 placed on ϕ , d_p and τ denote values corresponding to $F=0$ and $F=1$, respectively. The exponents n_d and n_τ were obtained from flow-through experiments of the partially oxidized UD_3 bed (Shugard et al., 2011). They were found to be equal to 2 and 1, respectively. The pore size and tortuosity corresponding to these two extremes, $F=0$ and $F=1$, were determined by fitting the fluid dynamics model to results from flow-through experiments, where D_2 stored in a small vessel is allowed to flow through the bed and exhaust to a vacuum pump. The pressure decay in the D_2 vessel reflects the permeability of the bed, i.e., as the permeability decreases so does the rate of pressure decay. These flow-through experiments were conducted after loading and hydriding the bed, and after the bed was fully oxidized (Shugard et al., 2011). Similarly, flow-through experiments were conducted for the case where only the frits were present in the reactor to determine the pore size and tortuosity for the frits. The results for the bed are: $d_{p,0} = 1.9 \times 10^{-4} \text{ cm}$, $\tau_0 = 1.693$, $d_{p,1} = 0.7 \times 10^{-4} \text{ cm}$, and $\tau_1 = 2.16$. Note that this constitutes a reduction in permeability of almost a factor of 20 due to the transition from the initial hydrided state to the fully oxidized state. The values for the frits are $\phi_f = 0.3$, $d_{p,f} = 7.5 \times 10^{-4} \text{ cm}$, and $\tau_f = 1.85$.

3.2. Finite element formulation

The governing equations described above were solved using the finite element method. The experiments were carried out by storing O_2 at an elevated pressure in a small vessel, and then allowing this O_2 to flow through the reactor. Thus, the pressure in the small vessel decreases such that the flow rate is a maximum at the beginning and monotonically decreases with time. The simulations of the experiments are carried out in the same way, the part of the model representing the small vessel is initially prescribed to contain pure O_2 at elevated pressure, and as the O_2 flows through the reactor, both the pressure in the small vessel and the flow rate through the reactor decrease with time. The gas in the small vessel is assumed to be isothermal. The thermo-physical properties of the solid and gas species in different simulation sub-domains are summarized in Table 2.

3.2.1. Boundary conditions

The reactor walls are impermeable, there is symmetry at the axis of the reactor, and there is a time dependent pressure specification at the outlet to the reactor. This time dependent pressure boundary condition is based on measurements taken during the experiments. Convection-like boundary conditions were applied at the location of the gas tight seals (see Fig. 1) to simulate their contact with the reactor wall. The heat flux at the

Table 1
Physical properties of the species present in the model (Edwards, 1969; White, 1991).

	O_2	D_2	UD_3	U	U_3O_8
M (g mol ⁻¹)	32	4	244	238	842
ρ (g cm ⁻³)	cM_{O_2}	$\rho - cM_{O_2}$	10.95	19.1	8.38
C_p (J mol ⁻¹ K ⁻¹)	$1.664 + 10.69 \log_{10}(T)$	$7.07 + 7.9 \times 10^{-4} T(^{\circ}C)$	49.3	27.7	238
μ (g cm ⁻¹ s ⁻¹)	1.92×10^{-4}	1.192×10^{-4}	–	–	–

Table 2

The thermophysical properties used in the different simulation domains.

	Ω_1	Ω_2	Ω_3	Ω_4
k (W cm ⁻¹ K ⁻¹)	$1.63 \times 10^{-4} \left(\frac{T}{273}\right)^{0.73}$	0.01	0.1	0.15
c_p (J g ⁻¹ K ⁻¹)	$\sum_{i=O_2, D_2} \frac{\rho_i}{\rho} c_{p,i}$	$\frac{\sum_{i=UD_3, U, U_3 O_8} C_{p,i} x_i}{\sum_{i=UD_3, U, U_3 O_8} M_i x_i}$	0.5	0.5
μ (g cm ⁻¹ s ⁻¹)	$\sum_{i=O_2, D_2} \mu_i x_i \left(\frac{T}{273}\right)^{0.68}$	$\sum_{i=O_2, D_2} \mu_i x_i \left(\frac{T}{273}\right)^{0.68}$	$\sum_{i=O_2, D_2} \mu_i x_i \left(\frac{T}{273}\right)^{0.68}$	–
ρ (g cm ⁻³)	$\frac{P}{RT} M_{D_2} + c(M_{O_2} - M_{D_2})$	$n_{bed} \sum_{i=UD_3, U, U_3 O_8} M_i x_i$	6.26	7.92
κ (cm ²)	10^{-3}	$\frac{\phi d_p^2}{\tau^2} \left(\frac{1}{32} + \frac{5}{12} Kn\right)$	$\frac{\phi_f d_{pf}^2}{\tau_f^2} \left(\frac{1}{32} + \frac{5}{12} Kn\right)$	–
\mathcal{D} (cm ² s ⁻¹)	$\frac{1.25}{P(\text{atm})} \left(\frac{T}{400}\right)^{1.404}$	$\frac{1.25 \phi_0}{P(\text{atm})} \left(\frac{T}{400}\right)^{1.404}$	$\frac{1.25 \phi_f}{P(\text{atm})} \left(\frac{T}{400}\right)^{1.404}$	–
ϕ	–	ϕ	ϕ_f	–

seal is given by:

$$q(\text{W cm}^{-2}) = 0.2(T(^{\circ}\text{C}) - T_{\text{seal}}). \quad (34)$$

The seal temperature T_{seal} is equal to 28 and 39 °C at the upstream and downstream locations, respectively, such that a small temperature gradient was established in the reactor as the initial condition. This is due to the elevated temperature that was maintained in the downstream hardware during the experiments, to prevent condensation. Adiabatic boundary conditions were applied to the remaining lateral surfaces of the reactor wall. In reality there are heat losses to the environment, these losses are small compared to the heat conducted into surfaces where the convection-like boundary conditions are applied. The boundary conditions on the O_2 transport equation are that the reactor walls are impermeable and there is a zero concentration gradient at the outlet. There is substantially more hardware attached to the reactor for fixturing and gas handling purposes in the experiments than represented by this model. This extra hardware behaves as an additional heat sink to the reactor. Its effect on the thermal response in the model was approximately accounted for through the use of the heat flux boundary conditions described above.

3.2.2. Initial conditions

The O_2 source vessel is given an initial gas composition of pure O_2 and a pressure corresponding to the experiment to be simulated. This varied from 20 to 171 psia, depending on the experiment. The initial gas composition in the reactor is prescribed to be pure D_2 . The initial temperature was set to the room value ($T_{\text{init}} = 30$ °C). The reactor was loaded with 0.01193 moles (2.84 g) of U where the distance between the frits was 1.328 cm and the internal diameter of the reactor was 0.8 cm. After several hydriding/dehydriding cycles using D_2 , the uranium was converted to a fine powder of UD_3 resulting in an initial density $[UD_3]^0 = 0.0178 \text{ mol cm}^{-3}$.

3.3. Solution method

The equations were solved using the commercial finite element software, COMSOL 3.5a. The fine mesh elements inside the UD_3 bed and frits are second-order quadrilaterals for improved accuracy in the reaction region. The mesh extends into second order triangular elements to the remaining parts of the computational domain with a size growth factor of 1.1. The total number of the quadrilateral and triangular elements is 10,550 and 4609, respectively, such that the total number of degrees of freedom is 197,113. The mesh sensitivity was checked by multiplying the total number of elements by four and finding that the global result differed by less than 1%. An implicit scheme was used to

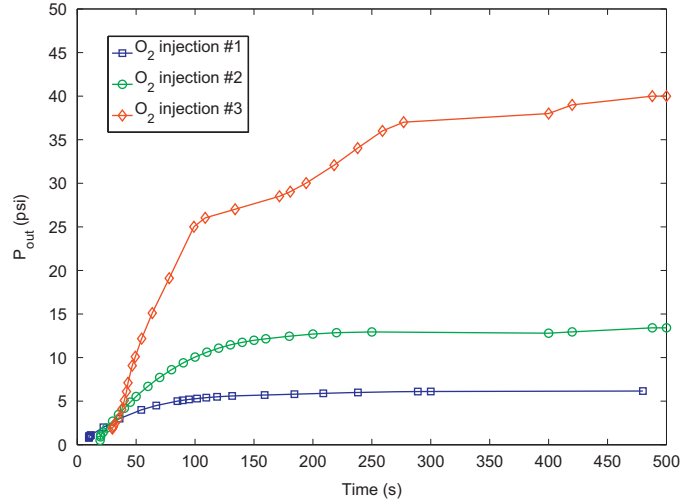


Fig. 2. Pressure evolution at the reactor gas outlet shown for the three O_2 injection experiments. These pressures were imposed as a boundary condition for Eq. (1) at the gas outlet surface depicted in Fig. 1.

integrate the transient system of PDEs and ODEs (Eqs. (1)–(6)) with a segregated solver at each time step (Hairer and Wanner, 1991; Comsol Multiphysics 3.5a: User's Guide, 2008). The PDEs are solved sequentially in the following order: Eqs. (1) and (3), (5), (2) then (6).

4. Results

The model was used to simulate three O_2 injection experiments (O_2 injection #1, #2 and #3). These experiments were carried out successively on a single reactor. In O_2 injection #1, only a small amount of O_2 was injected resulting in partial oxidation of the hydride material. In O_2 injection #2, a larger amount of O_2 was injected into the same reactor, but still leaving about 60% of the hydride material. In O_2 injection #3, excess O_2 was injected to completely oxidize the remainder of the hydride material. As mentioned in Section 2, the reacting bed was UD_3 instead of UH_3 . We expect that these results apply to both UH_3 and UD_3 beds.

The different amounts of O_2 used in each case result in different pressure profiles as a function of time at the reactor exit. These pressure profiles are shown in Fig. 2 for the three cases considered. Each pressure was imposed as boundary condition for Eq. (1) at the gas outlet.

4.1. O₂ injection #1

O₂ injection #1 used an O₂ source vessel with a volume of 45.0 ml and an initial pressure of 20 psia. Only 15% of the O₂ required to fully oxidize the bed to U₃O₈ was slowly injected over about 300 s. The O₂ was allowed to flow through the reactor and the effluent gas was collected in a 166.7 cm³ receiver vessel (Shugard et al., 2011). Fig. 3 shows a qualitative close-up of the bed region of the model, where it can be seen that a reaction front is predicted to evolve from at the leading edge of the hydride material. This front moves upward into the bed as time increases. The reaction rate is sufficiently large to consume all the O₂, such that the overall reaction rate is determined by the flow rate of O₂ into the hydride material. As the O₂ flow rate decreases with time ($t \geq 100$ s), both the thickness of the reaction front, and its propagation speed into the hydride material decrease.

The temperature and D₂ distributions in the vicinity of the hydride bed early in the process are shown in Fig. 4(a) and (b), respectively. A region of high temperature is coincident with the location of the UD₃ reaction front. Due to the slow O₂ injection rate, resulting from the low bed permeability, and due to the close proximity to the frit, which has a relatively large thermal conductivity, the temperatures that develop are not sufficiently high to decompose (dehydride) the UD₃ material. Consequently, the model predicts that only the UD₃ oxidation reaction occurs during O₂ injection #1. The D₂ concentration is largest at the interface between the leading frit and hydride material, where the reaction front was located at $t=4.5$ s (see Fig. 3). The D₂ concentration is also large downstream of that interface, and next to the reactor wall, but near the reactor axis it is lower due to the high temperature that exists there. Further downstream, the concentration decreases as the D₂ moves into regions of lower pressure. The figure also shows that due to the small flow velocity (typically 3 cm s⁻¹ near the leading edge of the bed) D₂ is able to diffuse upstream into the leading frit and towards the O₂ inlet channel leading to the bed. Fig. 4(c) shows the final UD₃ distribution predicted at the end of the first O₂ injection experiment. The deuteride material at the leading edge of the bed has been nearly completely consumed and converted to U₃O₈, while downstream of that region the UD₃ is still at its initial concentration.

The predicted and measured pressure decay in the O₂ source vessel during O₂ injection #1. At early times, the

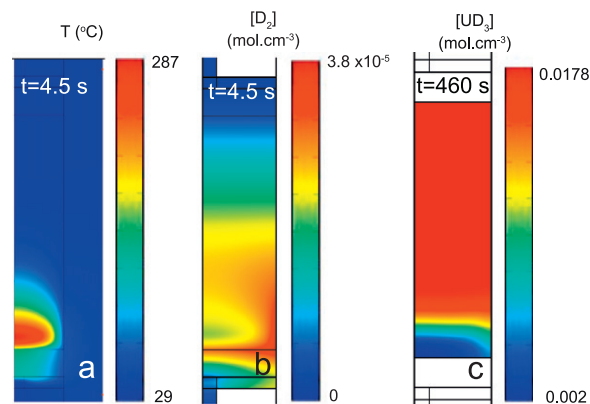


Fig. 4. Numerical predictions for: (a) the temperature, (b) the D₂ distribution in the vicinity of the bed, early in O₂ injection #1 at $t=4.5$ s, and (c) the final UD₃ distribution at the end of the experiment.

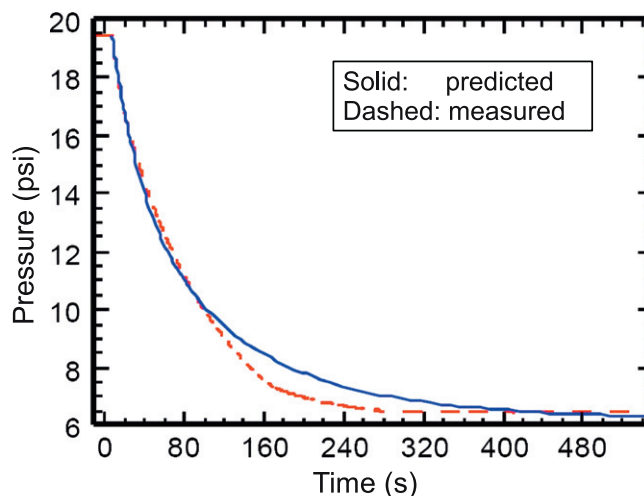


Fig. 5. The measured and predicted pressure decay in the gas source vessel during the first O₂ injection experiment.

model appears to predict the rate of pressure decay well, but later the predicted decay rate is smaller, indicating that the calculated bed permeability may be different than the actual value.

The temperature distribution in the hydride material on axis at various times is shown in Fig. 6(a). These represent the highest temperatures in the reactor due to the reaction. The frit provides enhanced conduction due to its relatively large conductivity compared to the hydride, such that the maximum temperature is located about 0.07 cm from the leading frit (located at $z=0$). There is some heat transfer, primarily by conduction, to other portions of the bed downstream resulting in elevated temperatures there. Fig. 6(b) shows the temperature as a function of time at the thermocouple locations (see Fig. 1). Although there are some differences between the calculated and measured results, they have an important similarity, and they both show that at the upstream location (TC #1) the maximum temperature is higher than that at the downstream location (TC #2). Based on the model, this is due to the confinement of the exothermic reaction and associated heat generation at the leading edge of the bed. (*i.e.*, the reaction forms a front as opposed to being distributed throughout the bed). The measured results appear to corroborate this behavior.

Fig. 7(a) and (b) shows the UD₃ concentration, ($\overline{[UD_3]}$) and the O₂ mole fraction ($\overline{[O_2]}$), respectively, averaged in the radial direction and plotted along the z direction in the vicinity of the leading edge of the bed. The $\overline{[UD_3]}$ profile at $t=1$ s is still near the initial

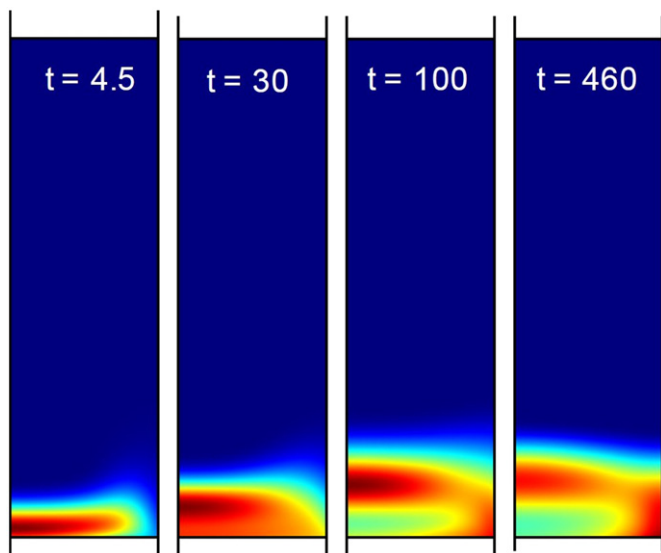


Fig. 3. A qualitative plot of the UD₃ oxidation reaction front R_{13} predicted by the model at various times for O₂ injection #1.

condition ($0.0178 \text{ mol cm}^{-3}$), and the profiles at later times show that $[\text{UD}_3]$ tends towards zero near the leading edge of the bed, but at positions downstream, $[\text{UD}_3]$ remains at the initial value. The \bar{x}_{O_2} profiles show that at the leading edge of the bed the gas is not pure O_2 due to the presence of D_2 , and that no O_2 exists downstream of $z \approx 0.35 \text{ cm}$. (i.e., all of the O_2 is consumed by the reaction front).

4.2. O_2 injection #2

The O_2 injection #2 experiment used a larger pressure (52 psia) in the O_2 source vessel. About 26% of the O_2 required to fully oxidize the bed to U_3O_8 was injected over $\sim 500 \text{ s}$. The initial state of the reactor for the second injection was the final state following O_2 injection #1, i.e., the leading $\sim 10\%$ of the bed was oxide. The larger source pressure creates a larger flow rate of O_2 into the reactor, and consequently a larger rate of UD_3 oxidation (reaction of Eq. (13)) and higher temperatures. This leads to UD_3 decomposition (reaction of Eq. (8)) and the formation of the U phase, which then leads to U oxidation (reaction of Eq. (12)). This can be seen in Fig. 8(a), (b) and (c) where the reactions fronts associated with the reactions of Eqs. (8), (12), and (13), respectively, are qualitatively shown 30 s after the beginning of O_2 injection #2. The initial UD_3 oxidation (not shown) is quite similar to the one shown in Fig. 3 for O_2 injection #1. In O_2 injection #2, that reaction creates large temperatures such that the decomposition of UD_3 takes place to form U near the axis. The UD_3 oxidation is confined to the near wall region and a U oxidation front exists near the axis. A UD_3 decomposition reaction front can be seen leading the two oxidation fronts as depicted in Fig. 8(b).

Fig. 9(a), (b), and (c) shows the temperature, U, and UD_3 distributions, respectively, early in O_2 injection #2. Gas flow streamlines are also shown with the temperature field. A perturbation to the streamlines can be seen in the region of high temperature created by the reactions, i.e., the gas expands as it flows through this region. A small region of U has been created by

UD_3 decomposition. The U is formed by a decomposition at the front of the leading edge of this region (upper side) and it is consumed by oxidation at its trailing edge (lower side). The UD_3 distribution at $t=30 \text{ s}$ shows the region where the concentration approached zero by decomposition and has been replaced by U. Later in the process, after the O_2 flow rate has decreased, the reaction rate and temperature in the bed decrease as well. Then,

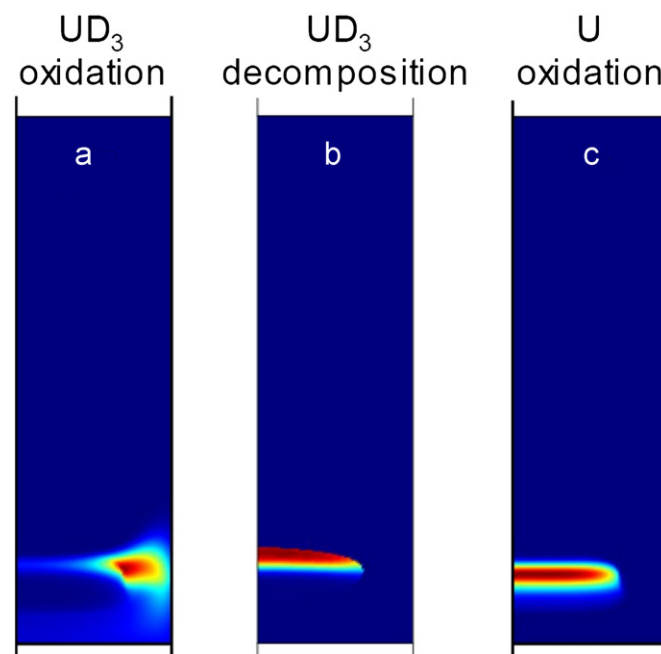


Fig. 8. A qualitative plot of the (a) UD_3 oxidation R_{13} front, (b) UD_3 decomposition R_8 front, and the (c) U oxidation R_{12} front, early ($t=30 \text{ s}$) in the simulation of O_2 injection #2.

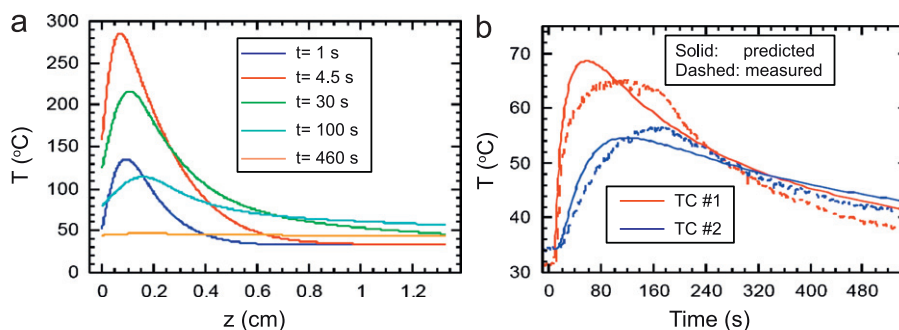


Fig. 6. (a) The predicted temperature profiles in the bed on axis ($r=0$) at various times, as indicated, and (b) a comparison of the predicted and measured temperatures at the locations of thermocouples TC #1 and TC #2.

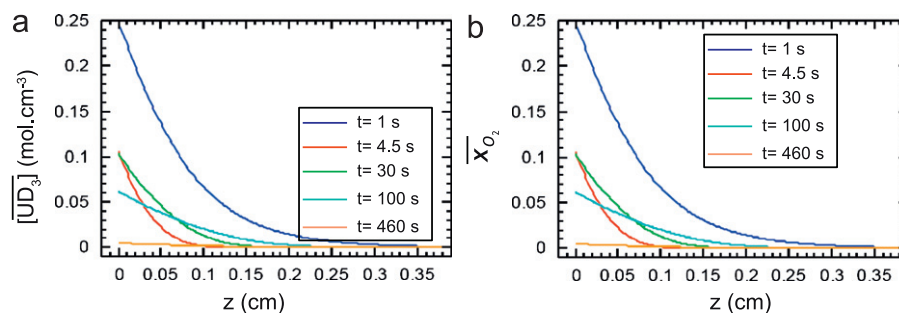


Fig. 7. The predicted (a) UD_3 concentration $[\text{UD}_3]$ and (b) O_2 mole fraction \bar{x}_{O_2} , averaged in the radial direction and plotted along the z -direction near the leading edge of the bed at various times.

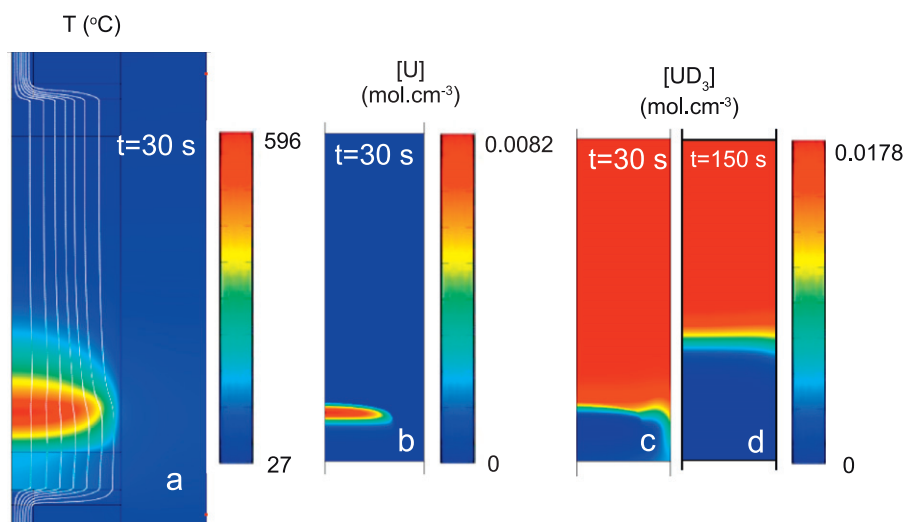


Fig. 9. Predictions of the (a) temperature (with flow streamlines), (b) U and (c) UD_3 distributions in the vicinity of the bed, early in O_2 injection #2, and (d) the final UD_3 distribution at the end of the experiment.

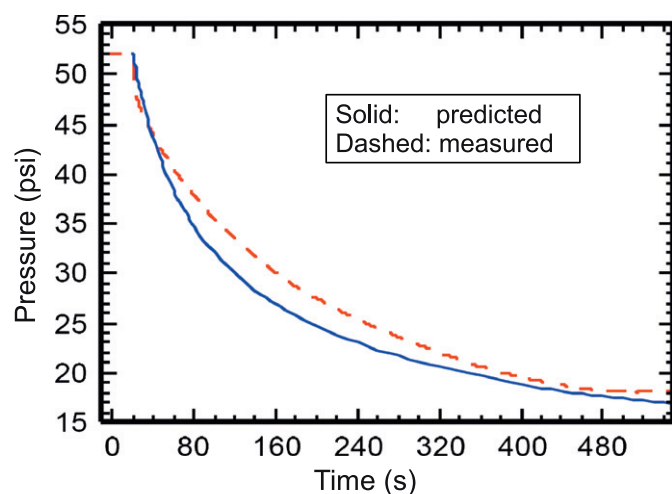


Fig. 10. Measured and predicted pressure decay in the gas source vessel during O_2 injection #2.

there is no decomposition, leaving UD_3 oxidation as the only reaction. The transition from pure UD_3 to pure U_3O_8 then resembles the one shown in Fig. 3 for O_2 injection #1, where it is approximately flat spanning from the reactor axis to the reactor wall. This leads to the final UD_3 distribution for O_2 injection #2 shown in Fig. 9(d) at $t=510$ s.

The predicted and measured pressure decay in the O_2 source vessel is shown in Fig. 10 for O_2 injection #2. The model in this case overpredicts the rate of pressure decay, indicating again that the calculated permeability may be different than the actual value. This is not surprising because Eqs. (31)–(33) used to calculate the permeability are based on a simplified model while in reality more complex processes are taking place in the bed and affecting the value of the permeability at different stages of the reaction.

The temperature distribution in the UD_3 material on the axis at various times is shown in Fig. 11(a). The results are similar to those shown in Fig. 6(a) for O_2 injection #1, except that the temperatures are much higher due to the faster O_2 flow rate. Fig. 11(b) shows the temperature as a function of time at the thermocouple locations. As was seen in O_2 injection #1, the maximum temperature at the upstream location (TC #1) occurs before the occurrence of the maximum temperature at the downstream location (TC #2), for both the measured and calculated results. However, here the measured

result shows the maximums at the two locations are nearly equal, while the model continues to show the maximum for TC #1 is larger than that for TC #2, as it did for O_2 injection #1. The measured result suggests a reaction front that is more spread out and centered between the two thermocouples than what was calculated in the model. There are different possible reasons for this discrepancy. First, the assumption, adopted in this model, that the U and UD_3 reactions have the same kinetics might not be general nor applicable to situations where both of these reactions happen at the same time. Second, the current model neglects swelling due to thermal and phase expansion in the UD_3 bed. Swelling induces non-uniform strain distribution throughout the bed leading to a non-uniform porosity. Finally, sharp changes in the bed porosity and permeability could occur near the contact surface between the bed and its housing leading to bed sintering and flow channeling.

The reaction rates \bar{R} , averaged in the radial direction, are plotted along the axial z -direction of the bed as shown in Fig. 12(a), at various times. UD_3 oxidation is the only reaction that takes place at early times ($t=20$ s), and it is fairly broad in its extent over the bed. The heat produced by this reaction decomposes the hydride near the axis such that UD_3 oxidation is partially replaced by a UD_3 decomposition front followed by a U oxidation front later on ($t=30$ s). At later times ($t \geq 150$ s), after the O_2 flow rate has decreased, the slower reaction rates allow temperatures to fall below the decomposition temperature and the UD_3 oxidation reaction becomes the only reaction on axis. The integral of the reaction rates over the bed, Ψ , is shown in Fig. 12(b) as a function of time, along with O_2 flow rate (multiplied by $\frac{3}{4}$ to allow for a more direct comparison between its values and the reaction rates, (i.e., one mole of UD_3 or U is consumed for every $\frac{4}{3}$ mole of O_2 consumed)). All rates are largest at the beginning when the O_2 source pressure is large and the flow rate is higher. At early times, the O_2 is consumed by a combination of UD_3 and U oxidation, where UD_3 decomposition takes place as well to produce the U. At later stages, only UD_3 oxidation remains and it becomes equal to the $\frac{3}{4}$ O_2 injection rate.

Fig. 13 shows the UD_3 and U concentrations ($\overline{[\text{UD}_3]}$ and $\overline{[\text{U}]}$) averaged in the radial direction and plotted along the z -direction of the bed. The UD_3 concentration profiles show the front that divides the portion of the bed that has been fully depleted of UD_3 (lower values of z) from the one that is still at its initial value ($0.0178 \text{ mol cm}^{-3}$), they suggest that this front propagates from

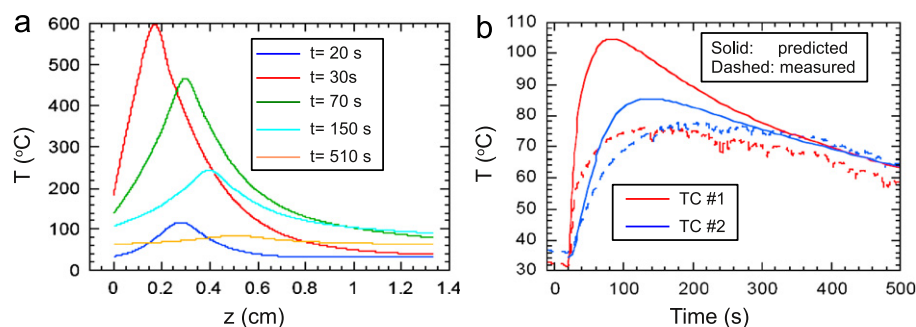


Fig. 11. For O_2 injection #2, (a) the predicted temperature profiles in the bed on axis at various times, and (b) a comparison of the predicted and measured temperatures at the locations of the thermocouples (see Fig. 1).

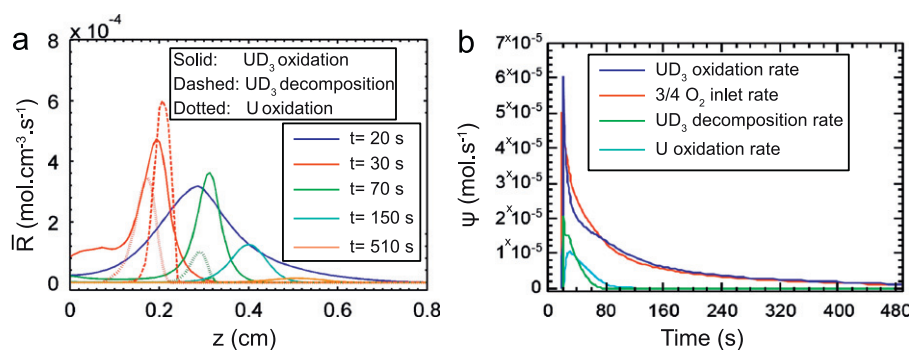


Fig. 12. For O_2 injection #2, the predicted results of (a) the reaction rates \bar{R} averaged in the radial direction and plotted in the axial z -direction of the bed, and (b) the integral Ψ of the reaction rates over the entire bed as functions of time.

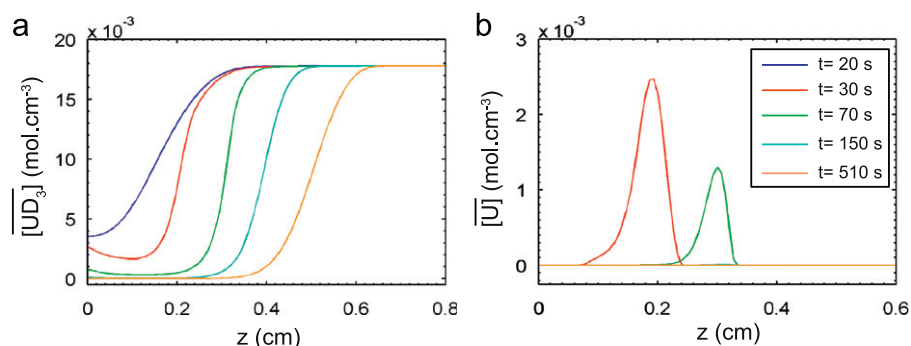


Fig. 13. The calculated (a) UD_3 concentration $[UD_3]$ and (b) U concentrations $[U]$, averaged in the radial direction.

left to right. Fig. 13(b) shows that U is present for the time period including $t=30$ and 70 s.

4.3. O_2 injection #3

For this experiment, 150% of the O_2 required to fully oxidize the bed to U_3O_8 was injected over ~ 500 s. O_2 injection #3 used a larger pressure (171 psia) in the O_2 source vessel than the prior two injection experiments. The initial state of the reactor for O_2 injection #3 was the final state following O_2 injection #2, i.e., the leading $\sim 38\%$ of the bed was oxide. The large source pressure creates large O_2 flow rates, reaction rates, temperatures, and significantly more UD_3 decomposition. In addition, this experiment made use of a 150 cm^3 helium reservoir driving a movable piston to maintain a large O_2 pressure throughout the flow injection process (Shugard et al., 2011).

Fig. 14(a), (b–d), (e) and (f) shows the temperature, reaction rates, UD_3 and U concentrations, respectively, early in the O_2

injection #3 simulation ($t=44$ s). Similarly to the results for O_2 injection #2, there is a short development period (not shown) that leads to a UD_3 oxidation front. This front is confined to a small region adjacent to the wall because all of the UD_3 has been replaced with U near the axis. The UD_3 decomposition front and the trailing U oxidation front then span most of the width of the bed. A significant portion of the bed is composed of U at this time. The U is formed at the leading edge (upper side) of this region by decomposition and it is consumed by oxidation at its trailing edge (lower side).

The measured and predicted pressure decay in the O_2 source vessel is shown in Fig. 15. Note that as the helium reservoir drives the piston sweep of the O_2 reservoir, the O_2 pressure remains large throughout the injection process. The model did not include the piston; rather a source volume equal to the sum of the helium and O_2 reservoir volumes was used, where the flow of O_2 into the reactor stopped when the pressure fell below 147 psia corresponding to the injection of an amount of gas that is initially on

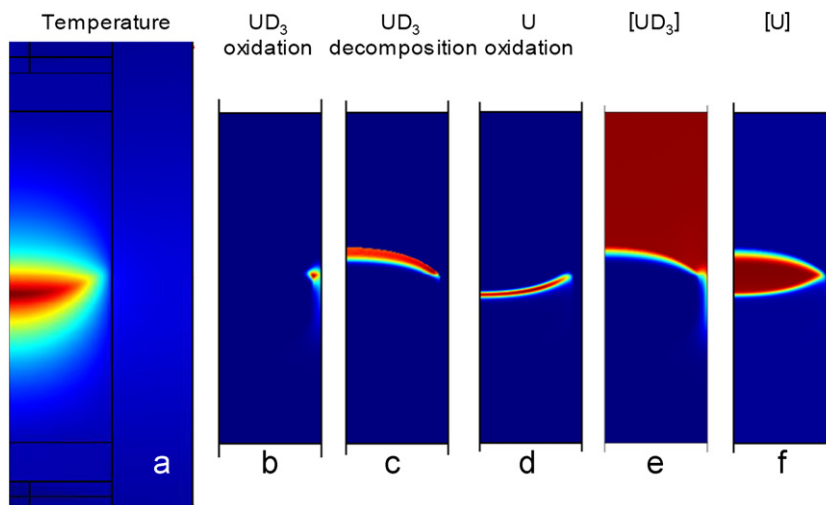


Fig. 14. A qualitative plot of numerical predictions of the (a) temperature, (b) UD_3 oxidation front R_{13} , (c) UD_3 decomposition front R_8 , (d) U oxidation front R_{12} , (e) UD_3 , and (f) U concentrations in the vicinity of the bed at $t=44$ s in O_2 injection #3.

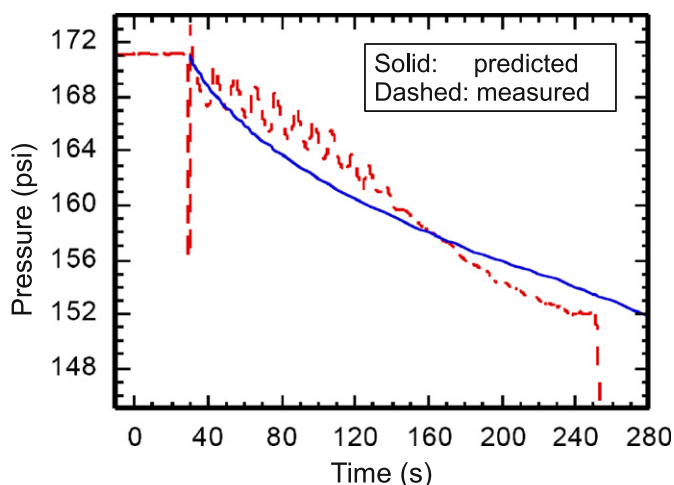


Fig. 15. The measured and predicted pressure decay in the gas source vessel during O_2 injection #3.

the O_2 side of the piston. The model underpredicts the rate of pressure decay, indicating that the calculated permeability may be different than the actual value.

The temperature distribution in the UD_3 material on the axis at various times is shown in Fig. 16(a). The results are similar to those for the prior two O_2 injections, except that the temperatures are much higher here due to the faster O_2 flow rate. Note that the maximum temperature decreases with time not because of a decrease in O_2 flow rate, as that is almost constant throughout O_2 injection #3, but rather due to the proximity of the downstream frit (located at $z=1.33$ cm), which has a relatively large conductivity. Fig. 16(b) shows the temperature as a function of time at the thermocouple locations. In contrast to the prior two O_2 injections, the maximum temperature at the upstream location (TC #1) is smaller than that at the downstream location (TC #2), for both the measured and calculated results. This is consistent with a sharp reaction front propagating across the bed, where here the reaction front is closer to the downstream position making it hotter. There is significant disagreement between the calculated and measured results shapes of the temperature curves. The cause of this is uncertain, but it may be related to

heat transfer effects in the hardware present in the experiment but absent in the model.

The reaction rates, \bar{R} , averaged in the radial direction are plotted along the z -direction of the bed as shown in Fig. 17(a), at various times. UD_3 oxidation is dominant at early ($t=32$ s) and late ($t=235$ s) stages of the injection, when the temperature is sufficiently small such that decomposition has not depleted the majority of the UD_3 . The integral of the reaction rates over the bed, Ψ , is shown in Fig. 17(b) as a function of time, along with O_2 flow rate (multiplied by $\frac{3}{4}$). Throughout most of the injection, UD_3 decomposition and oxidation and U oxidation occur. Interestingly, the average decomposition rate is the largest at early times. All the reactions stop at $t=235$ s because all the UD_3 and U are consumed in the bed. Note that UD_3 oxidation is the last to stop due to the reduction in temperature as the reaction approaches the downstream frit. The O_2 flow rate increases after that because the temperature, and hence gas viscosity, decrease.

For all cases except O_2 injection #3, the experimental results showed that there was no O_2 present in the effluent gas exiting the reactor. The results for O_2 injection #3 is shown in Fig. 18. The measured results show that at $t=160$ s the gas composition switches from being mostly D_2 to mostly O_2 . The simulated result shows similar behavior except it does not happen until $t=220$ s. This is consistent with the source pressure results shown in Fig. 15, where the model underpredicted the pressure decay rate, and suggests the permeability is underpredicted as well. Fig. 18(a) shows the same results, except with a shift in the time scale of the calculated results to allow for an easier comparison to the measured results. The measured rate of the gas composition transition from D_2 to O_2 is well matched by the simulated result. The agreement seen in Fig. 18 provides some confidence for the kinetic parameters used in this model.

5. Conclusion

In this paper, a multiphysics finite element model was developed for the reaction of oxygen gas and uranium hydride within a hydrogen storage bed. The model explicitly considered rates of chemical reaction, heat transport, and mass transport within a deuteride bed. The model was applied to three oxygen injection cases, and the predictions were compared to experimental measurements.

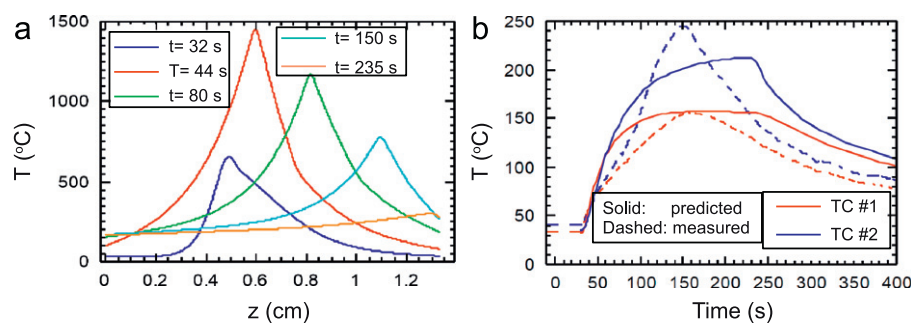


Fig. 16. (a) The predicted temperature profiles in the bed on axis at various times, and (b) a comparison of the predicted and measured temperatures at the locations of the thermocouples for O_2 injection #3.

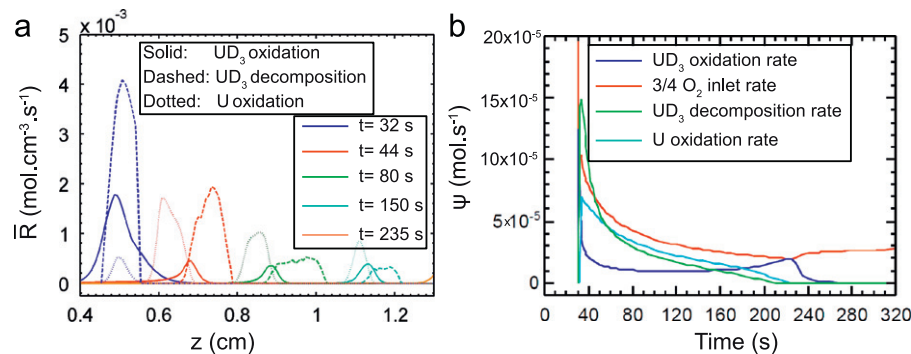


Fig. 17. The calculated results for (a) the reaction rates \bar{R} averaged in the radial direction and plotted along the z -direction, and for (b) the integral Ψ of the reaction rates over the entire bed as functions of time for O_2 injection #3.

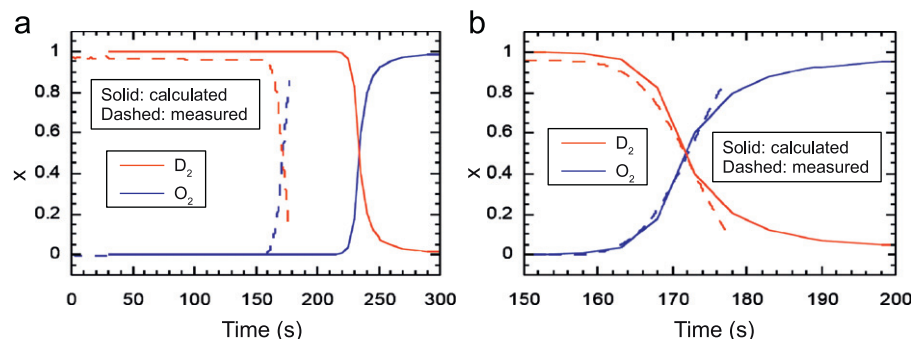


Fig. 18. The gas composition exiting the reactor for the third O_2 injection. (a) Results presented using as-measured and as-calculated time scales. (b) Results presented after shifting the calculated time scale for better comparison of the composition rates with the measured results.

We find that the $UD_3 + O_2$ reaction is significantly faster than what the literature reports of the $U + O_2$ reaction near room temperature. In fact, the $UD_3 + O_2$ reaction is found to be fast enough that, under the conditions studied, oxidation reactions are concentrated in a thin front that advances through the bed. We also find that under the conditions studied, uranium hydride reacts completely with oxygen, without passivation. Hydrogen is produced by direct conversion of UD_3 to U_3O_8 , and, at faster rates of oxygen injection, by UD_3 decomposition caused by high local temperatures in the vicinity of the reaction front.

It is also found that oxidation of UD_3 to U_3O_8 produces significant material swelling, which, in this reactor, reduces the porosity from approximately 0.60 to 0.39. This, in-turn, decreases the bed permeability by a factor of almost 20. A simple, yet reasonably general, description of this process was proposed, which appears to capture the majority of this local expansions influence on the global bed flow properties. The model described here will be useful to better anticipate the effects of air ingress on uranium hydride storage beds and for exploring design options for

hydrogen generation systems—without the expense and hazards associated with experimental work. While we used deuterium in our study, we expect the results and model to be applicable to hydrogen as well because the isotopes are chemically similar.

The model has already helped in identifying important design features for a uranium hydride based hydrogen generating reactor. Ultimately, desirable reactor characteristics include: a capability to accept a range of oxygen injection rates, the complete consumption of oxygen, and maximum reactor wall temperatures that remain well below material softening thresholds. It is clear from this work that these characteristics may require more elaborate designs than were used in the experiments described herein. For example, hardware that distributes the oxygen throughout the hydride bed may be necessary. Additionally, it may be worthwhile to consider mixing an unreacting diluent, e.g., U_3O_8 or Al_2O_3 , with the uranium hydride powder to reduce local maximum temperatures and also reduce the magnitude of oxidation induced permeability changes. The model developed here could be used to test ideas such as these relatively easily and quickly.

Although the present model development and findings appear promising, additional research is needed to further strengthen the underlying methodology, to extend its scope, and address remaining unknowns. For example, a more rigorous experimental study is required to obtain more accurate reaction kinetics for uranium hydride oxidation. In addition, the bed swelling and permeability model could be improved to better describe the phase expansions and subsequent permeability changes observed in the experiments.

Nomenclature

D	diffusivity ($\text{cm}^2 \text{s}^{-1}$)
c	oxygen molar concentration (mol cm^{-3})
c_p	specific heat, mass based ($\text{J g}^{-1} \text{K}^{-1}$)
C_p	specific heat, mole based ($\text{J mol}^{-1} \text{K}^{-1}$)
d_p	pore size (cm)
d_{O_2}	oxygen molecule diameter (cm)
E	oxidation activation energy (J mol^{-1})
F	fraction of the bed that is oxidized
k	thermal conductivity ($\text{W cm}^{-1} \text{K}^{-1}$)
Kn	Knudsen number
M	molecular weight (g mol^{-1})
n	molar density (mol cm^{-3})
P	gas pressure ($\text{g s}^{-2} \text{cm}^{-1}$)
Q	energy source term (W cm^{-3})
q	heat flux (W cm^{-2})
R	reaction/decomposition rate ($\text{mol cm}^{-3} \text{s}^{-1}$)
S	mass source term ($\text{g cm}^{-3} \text{s}^{-1}$)
T	temperature (K)
V	gas velocity (cm s^{-1})
x	mole fraction

Chemical components

D_2	deuterium
O_2	oxygen
U	uranium
U_3O_8	triuranium octoxide
UD_3	uranium deuteride
UH_3	uranium hydride

Greek letters

α	decomposition rate constant (s^{-1})
β	oxidation rate constant (s^{-1})
ΔH	enthalpy of reaction (J mol^{-1})
Δv	solid volume expansion upon changing from hydride to oxide
κ	permeability (cm^2)
λ	mean free path (cm)
μ	gas viscosity ($\text{g cm}^{-1} \text{s}^{-1}$)
ϕ	porosity
ρ	total mass density of gas (g cm^{-3})
τ	tortuosity
θ	decomposition activation temperature (K)

Subscripts

eq	equilibrium
0,1	initial and partially oxidized bed
(8), (12), (13)	reactions described by Eqs. (8), (12) and (13)
f	frits
$\text{O}_2, \text{UD}_3, \text{U}$	terms in Eqs. (3), (5), and (6)

Superscripts

0	initial value, or all hydride phase
---	-------------------------------------

Acknowledgements

George Buffleben, Ken Stewart, David Shimizu, Toff Garcia and Albert Sandoval provided technical assistance that was crucial to the completion of this work. David Robinson, Scott James and Bernice Mills provided valuable discussions and feedback that were helpful to accomplish this work.

This work was supported by the Laboratory Directed Research and Development (LDRD) and Advanced Simulation and Computing Physics and Engineering Models (ASC-PEM) programs at Sandia National Laboratories.

Sandia National Laboratories is a multi-program laboratory managed and operated by Sandia Corporation, a wholly owned subsidiary of Lockheed Martin Corporation, for the U.S. Department of Energy's National Nuclear Security Administration under contract DE-AC04-94AL85000.

References

- Abraham, B.M., Flotow, H.E., 1955. The heats of formation of uranium hydride, uranium deuteride and uranium tritide at 25 °C. *J. Am. Chem. Soc.* 77 (6), 1446–1448.
- Antoniuzzi, A.B., et al., 2008. High-pressure and high-temperature tritium apparatus for the tritiation of materials. *Fusion. Sci. Technol.* 54 (2), 635.
- Antonio, R.F., Sarrate, J., Huerta, A., 2003. Numerical modelling of void inclusions in porous media. *Int. J. Numer. Meth. Eng.* 59 (4), 577–596.
- Balasubramanian, K., Siekhaus, W.J., McLean II, W., 2003. Potential energy surfaces for the uranium hydriding reaction. *J. Chem. Phys.* 119 (12), 5889.
- Bird, R.B., Stewart, W.E., Lightfoot, E.N., 1960. *Transport Phenomena*. Wiley & Sons, Inc.
- Bowman, C.C., Vis, V.A., 1990. Tritium handling facility at KMS fusion inc. *J. Vac. Sci. Technol. A* 8 (3), 2890.
- Coffin, D.O., 1988. Safe tritium handling at the tritium systems test assembly. *J. Vac. Sci. Technol. A* 6 (3), 1264.
- Comsol Multiphysics 3.5a: User's Guide. Comsol, 2008.
- Condon, J.B., 1980. Nucleation and growth in the hydriding reaction of uranium. *J. Less. Common Mat.* 73, 105–112.
- Condon, J.B., Larson, E.A., 1973. Kinetics of the uranium-hydrogen system. *J. Chem. Phys.* 59, 855.
- Edwards, A.L., 1969. A Compilation of Thermal Property Data for Computer Heat Conduction Calculation. Internal Report. Lawrence Radiation Laboratory.
- Epstein, M., et al., 1996. On prediction of the ignition potential of uranium metal and hydride. *Nucl. Safety*, 37, 12.
- Gill, J.T., et al., 1983. Tritium storage/delivery and associated cleanup systems for TFTR. *J. Vac. Sci. Technol. A* 1 (2), 856.
- Hairer, E., Wanner, G., 1991. *Solving Ordinary Differential Equations II, Stiff and Differential-Algebraic Problems*. Springer-Verlag.
- Hayashi, T., et al., 2008. Safe handling experience of a tritium storage bed. *Fusion. Eng. Des.* 83, 1429.
- Heung, L.K., 1995. Tritium transport vessel using depleted uranium. *Fusion. Technol.* 28 (3), 1385.
- Khaled, A.-R.A., Vafai, K., 2003. The role of porous media in modeling flow and heat transfer in biological tissues. *Int. J. Heat Mass. Trans.* 46, 4989–5003.
- Lasser, et al., 1999. Overview of the performance of the JET active gas handling system during and after dte1. *Fusion. Eng. Des.* 47, 173.
- Le Guyader, F., et al., 2010. Pyrophoric behaviour of uranium hydride and uranium powders. *J. Nucl. Mater.* 396, 294.
- Lide, D.R., 2004. *CRC Handbook of Chemistry and Physics*. CRC Press.
- Lindner, D.L., 1990. Isothermal decomposition of uranium hydride. *J. Less. Common Metals* 157, 139.
- Longhurst, G.R., 1988. Pyrophoricity of tritium-storage bed materials. *Fusion. Technol.* 14, 750.
- Longhurst, G.R., 1990. The INEL tritium research facility. *Fusion. Eng. Des.* 12, 403.
- Longhurst, G.R., et al., 1992. Experimental evaluation of the consequences of uranium bed air-ingress accidents. *Fusion. Technol.* 21, 1017.
- Longhurst, G.R., Shmayda, W.T., 1995. Uranium storage bed accident hazards evaluation. In: *IEEE Thirteenth Symposium on Fusion Engineering*, vol. 1, p. 812.
- Manchester, F., San-Martin, A., 1995. The H-U (hydrogen-uranium) system. *J. Phase Equil.* 16, 263.
- Mason, E.A., Malinauskas, A.P., 1983. Gas transport in porous media: the dusty gas model. In: *Chemical Engineering Monographs*, Elsevier.
- McEachern, R.J., Taylor, P., 1998. A review of the oxidation of uranium dioxide at temperatures below 400 °C. *J. Nucl. Mater.* 254 (2–3), 87–121.
- McWhorter, S., et al., 2011. Materials-based hydrogen storage: attributes for near-term, early market PEM fuel cells. *Curr. Opin. Sol. State. Mater. Sci.* 15, 29.
- Ortman, M.S., et al., 1990. Tritium processing at the savannah river site: present and future. *J. Vac. Sci. Technol. A* 8 (3), 2881.
- Perevezentsev, A.N., et al., 1995. Safety aspects of tritium storage in metal hydride form. *Fusion. Technol.* 28, 1404.

- Powell, G.L., 2004. Reaction of oxygen with uranium hydride. In: *Advanced Materials for Energy Conversion*, Chandra.
- Ritchie, A.G., 1981. A review of the rates of reaction of uranium with oxygen and water vapour at temperatures up to 300 °C. *J. Nucl. Mater.* 102, 170–182.
- Robinson, S.L., Thomas, G.J., 1996. Uranium hydride formation and properties: a review with commentary on handling and disposition. Report SAND1996-8206, Sandia National Laboratories.
- Shmayda, W.T., Mayer, P., 1984. Uranium beds for temporary tritium storage. *J. Less. Common Mater.* 104 (2), 239.
- Shugard, A.D., Buffleben, G.M., Kanouff, M.P., James, S.C., Robinson, D.B., Mills, B.E., Gharagozloo, P.E., Van Blarigan, P., 2011. Rapid Hydrogen Gas Generation Using Reactive Thermal Decomposition of Uranium Hydride. Report SAND2011-6939, Sandia National Laboratories.
- Totemeier, T.C., 2000. Characterization of uranium corrosion products involved in a uranium hydride pyrophoric event. *J. Nucl. Mater.* 278 (2–3), 301.
- Totemeier, T.C., Hayes, S.L., 1996. Analytical and numerical models of uranium ignition assisted by hydride formation. In: *DOE Spent Nuclear Fuel and Fissile Material Management Conference*.
- Totemeier, T.C., Pahl, R.G., Frank, S.M., 1999. Oxidation kinetics of hydride-bearing uranium metal corrosion products. *J. Nucl. Mater.* 265, 308.
- Vafai, K., 2005. *Handbook of Porous Media*. Taylor & Francis.
- Walthers, C.R., 1984. Description and performance of uranium beds used to pump tritium–deuterium at the tritium systems test assembly. *J. Vac. Sci. Technol. A* 1 (2), 722.
- White, F.M., 1991. *Viscous Fluid Flow*. McGraw-Hill, New York, NY.
- Young, J.B., Todd, B., 2005. Modelling of multi-component gas flows in capillaries and porous solids. *Int. J. Heat Mass. Trans.* 48, 5338.